Time-dependent nonequilibrium soft x-ray response during a spin crossover

Michel van Veenendaal

Time-dependent nonequilibrium soft-X-ray response during a spin crossover

Michel van Veenendaal[1, 2, *]

[1]*Department of Physics, Northern Illinois University, DeKalb, Illinois 60115, USA*
[2]*Advanced Photon Source, Argonne National Laboratory,*
9700 South Cass Avenue, Argonne, Illinois 60439, USA
(Dated: February 20, 2018)

A theoretical framework is developed for better understanding the time-dependent soft-X-ray response of dissipative quantum many-body systems. It is shown how X-ray absorption and resonant inelastic X-ray scattering (RIXS) at transition-metal L-edges can provide insight into ultrafast intersystem crossings of importance for energy conversion, ultrafast magnetism, and catalysis. The photoinduced doublet-to-quartet spin crossover on cobalt in Fe-Co Prussian blue analogues is used as an model system to demonstrate how the X-ray response is affected by the nonequilibrium dynamics on a femtosecond timescale. Changes in local spin and symmetry and the underlying mechanism are reflected in strong broadenings, a collapse of clear selection rules during the intersystem crossing, fluctuations in the isotropic branching ratio in X-ray absorption, crystal-field collapse/oscillations, and time-dependent anti-Stokes processes in RIXS.

I. INTRODUCTION

Understanding intersystem crossings on a femtosecond timescale is of the upmost importance for progress in fields such as ultrafast magnetism and phase transitions, catalysis, and energy conversion processes. Unfortunately, few experimental tools allow the measurement of the nonequilibrium electronic structure on this timescale. Recent years have seen the construction of several X-ray free-electron laser facilities based on the principle of self-amplified spontaneous emission enabling the creation of femtosecond X-ray pulses with a few hundred meV resolution. By using the self-seeding mechanism[1–3], additional spectral power and stability can be obtained. Despite the tremendous experimental progress, our understanding of the nonequilibrium X-ray response function is virtually uncharted territory, which complicates experimental progress and hampers our ability to extract information from these crucial experiments. In this Letter, it is demonstrated that X-ray spectroscopy can provide valuable insights into the changes in local spin and electronic structure on a femtosecond timescale. This ability is demonstrated by the study of an ultrafast spin crossover[4–7], a model intersystem crossing where the local moment is changed on the femtosecond timescale after irradiation with visible light. Recent experiments have pushed the spin crossover switching time below 50 fs[8], which is less than the oscillation period of the breathing mode of the ligands surrounding the magnetic ion. In addition to potential applications in magnetic data storage, spin crossover materials were one of the first systems studied using ultrafast X-ray based pump-probe experiments[9–12].

The X-ray response is described for the photoinduced spin crossover on the cobalt ion in Fe-Co Prussian blue analogues[13–15]. The process is initiated by a photoexcitation from the iron to the cobalt ion, see Fig. 1. Whereas the Fe ion remains low spin, the divalent cobalt ion goes from a doublet ($S = \frac{1}{2}$) to a quartet ($S = \frac{3}{2}$)[13,14,16]. The observed increase in the cobalt-ligand bond length oc-curs in less than half the oscillation period of the breathing mode[12]. The relative simplicity of the spin crossover in the Fe-Co Prussian blue analogues allows us to focus on the effects of intersystem crossings on the time-dependent nonequilibrium X-ray response. The most common soft-X-ray experiments that can probe the spin crossover are X-ray absorption (XAS) and resonant inelastic X-ray scattering RIXS) at the transition-metal L edges $(2p \rightarrow 3d)$[10,17–20]. Some progress has been made in the theoretical treatment of femtosecond spectroscopy using nondissipative *ab initio* methods[21–24] with classical nuclear motion. Whereas *ab initio* approaches often work well at K-edges, the agreement with experiment is usually poor at transition-metal L-edges that are dominated by configuration interactions. Here, an approach is taken where the emphasis lies on a proper many-body description of the Coulomb and spin-orbit interactions and a quantum-mechanical treatment of the dominant breathing mode representing the metal-ligand distance. The time-dependent XAS and RIXS show several key features that allow the study of the nonequilibrium dynamics.

II. MODEL

The model couples a cobalt ion with full configuration interaction to a breathing mode that describes the change in metal-ligand distance[15,25]. Quantum dissipation of the oscillation of the breathing mode causes a complete relaxation into the metastable high-spin state. This model has been successfully used to describe the low-to-high spin crossover in Fe-Co Prussian blue analogues[15]. The total Hamiltonian $\hat{H} = \hat{H}_{el} + \hat{H}_{el-phonon}$ contains an electronic and and an electron-phonon part. The electronic

part is given by

$$\hat{H}_{\text{el}} = \sum_{\mu\mu'}(\Delta_{\mu\mu'} + \zeta_\mu\langle\mu|\mathbf{L}\cdot\mathbf{S}|\mu'\rangle)c_\mu^\dagger c_{\mu'}$$
$$+ \sum_{\mu_1\mu_2\mu_3\mu_4} U_{\mu_1\mu_2\mu_3\mu_4}c_{\mu_1}^\dagger c_{\mu_2}^\dagger c_{\mu_3}c_{\mu_4} \quad (1)$$

where $c_\mu^\dagger$ creates an electron in an orbital with index $\mu = nlm\sigma$ where nlm are the usual quantum numbers of a hydrogen-like atom and $\sigma = \pm\frac{1}{2}$ is the spin projection. More details on the Hamiltonian and the spin crossover are given in[15]. For a divalent cobalt atom, the initial and RIXS final-state configurations are $|3d^7; n\rangle$ where n here refers to the number of excited states of the local breathing mode. The XAS final states and RIXS intermediate states are $|\underline{2p}3d^8; n\rangle$, where $\underline{2p}$ refers to a hole in the $2p$ core level. The first term on the right-hand side contains the single-particle interactions, such as on-site energies given by $\Delta_{\mu\mu'}$ and the $2p$ and $3d$ spin-orbit interactions $\mathbf{L}\cdot\mathbf{S}$. The second term contains the full multiplet Coulomb interaction between the $3d$ electrons and between the $3d$ electrons and the $2p$ core hole[26,27]. The electronic part of this many-body model has been very successful in describing spectroscopy on transition-metal compounds in the X-ray and optical region[26–30]. The parameters agree well with those used to interpret mixed-valence Fe-Co Prussian blue analogues[28] and the RIXS for divalent cobalt[31,32].

The dominant change in the interaction between the cobalt ion and the ligands is due to the increase in metal-ligand distance, which has by far the largest effect on the local electronic structure. Symmetry considerations tell us that the most important mode is the breathing mode where the distance between the cobalt and the ligands changes equally in all six directions. The coupling between the breathing mode and the local electronic structure is given by

$$\hat{H}_{\text{el-phonon}} = \hbar\omega_0 a^\dagger a - \sqrt{\varepsilon_p\hbar\omega_0}(a^\dagger + a)\frac{\alpha + \underline{n}_{t_2}}{\alpha + 1}, \quad (2)$$

where $\hbar\omega_0 = 40$ meV, $a^\dagger$ is the step-up operator for the breathing mode, and $\underline{n}_{t_2}$ is the number of t_2 holes. The last term on the right-hand side is the electrostatic interaction between the electrons and the breathing mode parametrized by the energy $\varepsilon_p = 2.5$ eV. There are two factors contributing to an increase in metal-ligand distance. First, the stronger repulsion resulting from the change in valence from trivalent to divalent is included by the term $\alpha = 2$. Second, the spin crossover happens via a $t_2 \rightarrow e$ conversion. Since the lobes of the e orbitals are pointing towards the ligands, the repulsion of an electron in this state and the negatively-charged ligands is stronger than that of the t_2 orbitals. This term is proportional to the number of t_2 holes $\underline{n}_{t_2}$ which is directly related to the number of e electrons, $n_e = 1 + \underline{n}_{t_2}$. The parameter values have been optimized to obtain agreement with *ab initio* potential landscapes[14,16] with regards to energy separations and relative equilibrium positions.

Dissipation is included through the damping of the motion of the breathing mode[15,25]. The physics underlying the damping is that the local vibronic mode is not an eigenstate of the larger system. The majority of the damping is therefore a simple delocalization of the oscillation, which represents itself as a damping in the model where only a local breathing mode is considered. In molecular spin-crossover complexes, this delocalization manifests itself nicely by a transfer of vibrational energy from the breathing to the bending modes[12]. This damping is essential for understanding the entire spin crossover process, since it removes excess energy from the local system and prevents recurrences to the original state. For larger time scales $t > 500$ fs) the damping of the breathing mode is not the most effective relaxation mechanism between the spin-orbit-split states of the lowest quartet state and the inclusion of additional relaxation processes, such as long-range Coulomb scattering, can reduce the relaxation time. However, the X-ray reponse is more dependent on the nature and symmetry of the lowest states and less on the relaxation mechanism. Therefore, the X-ray response is expected to be similar.

III. X-RAY SPECTRAL FUNCTIONS

For the X-ray response, we consider L-edge ($2p \rightarrow 3d$) spectroscopies, which are of importance for understanding experiments at self-seeded soft-X-ray free-electron lasers. These are strong transitions dominated by the dipole operator D_q, where q are the components. The X-ray absorption is calculated using Fermi's golden rule

$$I_{\text{XAS}}(\omega, t) = \sum_{n,q} |\langle n|D_q|\psi(t)\rangle|^2\delta(\hbar\omega + E(t) - E_n), \quad (3)$$

where $\hbar\omega$ is the energy of the incoming photon and a summation over the different polarization components q is made to obtain the isotropic spectrum. The initial state is the time-dependent wavefunction $|\psi(t)\rangle$ with energy $E(t) = \langle\psi(t)|\hat{H}|\psi(t)\rangle$; the final states $|n\rangle$ have energy E_n. The RIXS is obtained from the Kramers-Heisenberg formula[33],

$$I_{\text{RIXS}}(\omega, t) = \sum_{f,qq'}\left|\sum_n\frac{\langle f|D_{q'}|n\rangle\langle n|D_q|\psi(t)\rangle}{\hbar\omega + E(t) - E_n + i\frac{\Gamma}{2}}\right|^2$$
$$\times \delta(\hbar(\omega' - \omega) + E_f - E(t)), \quad (4)$$

where $\Gamma = 0.27$ eV is the lifetime broadening in the intermediate state. Note that the X-ray absorption final states are the intermediate states of the RIXS process. Since the core-hole lifetime is much shorter than the oscillation period of the breathing mode, the spectra are calculated as instantaneous. The energy difference $\hbar(\omega' - \omega)$ between the final and initial photon is equal to the energy $E(t) - E_f$, where negative and positive differences correspond to an energy loss and gain, respectively. Since
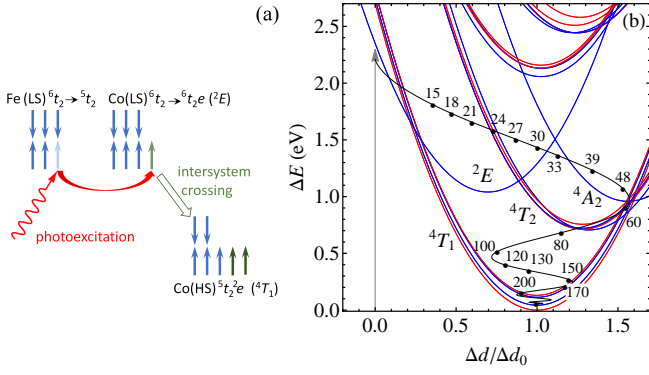
FIG. 1: (a) Schematic description of the spin crossover in Fe-Co Prussian blue analogues. The doublet-to-quartet intersystem crossing is initiated by a Fe to Co photoexcitation. (b) The schematic energy landscape by treating the breathing mode as classical. The energies are plotted as a function of the change in metal-ligand distance, where Δd_0 is the change in distance between the lowest states of Co^{3+} (low spin) and Co^{2+} (high spin). The red and blue energy curves indicate two- and four-fold degenerate states, respectively. The black line gives the total energy of the system (kinetic plus potential) as a function of the expectation value of the metal-ligand distance $\langle \Delta d(t) \rangle / \Delta d_0$. The numbers indicate times in femtoseconds for which the X-ray response is shown.

the RIXS process started from an excited state, the final photon energy $\hbar\omega'$ can exceed its initial value $\hbar\omega$.

The model was solved by constructing a matrix based on the Hamiltonian in Eq. (2) for the basis described in the Model Section. The time-development of the photoexcited state is calculated using Krylov subspace techniques[34]. Dissipation occurs via the inclusion of a microscopic damping mechanism of the vibronic mode as was described in detail in earlier work[15,25]. X-ray spectra are calculated by applying the dipole operator on the nonequilibrium state and performing a tridiagonalization. For RIXS, the dipole operator is applied again on the vectors obtained via tridiagonalization. A second tridiagonalization is then performed to obtain the RIXS final states.

IV. RESULTS

Figure 1 summarizes the key results of the spin crossover in Fe-Co Prussian blue analogues from Ref.[15]. In the ground state, both Fe^{2+} and Co^{3+} are in a low-spin t_2^6 configuration, see Fig. 1(a). The spin crossover is initiated by transferring an electron from the iron to the cobalt ion. The low-spin $t_2^6 e$ configuration (^2E in Mulliken notation) is a highly-excited state, see Fig. 1(b). Although the actual calculation uses a quantum-mechanical breathing mode, Figure 1(b) shows the more intuitive classical energy landscape. Around 15-20 fs, a crossing between the low-spin doublet and the high-spin $t_2^5 e^2$ ($^4T_1$) quartet state occurs. In the absence of quan-
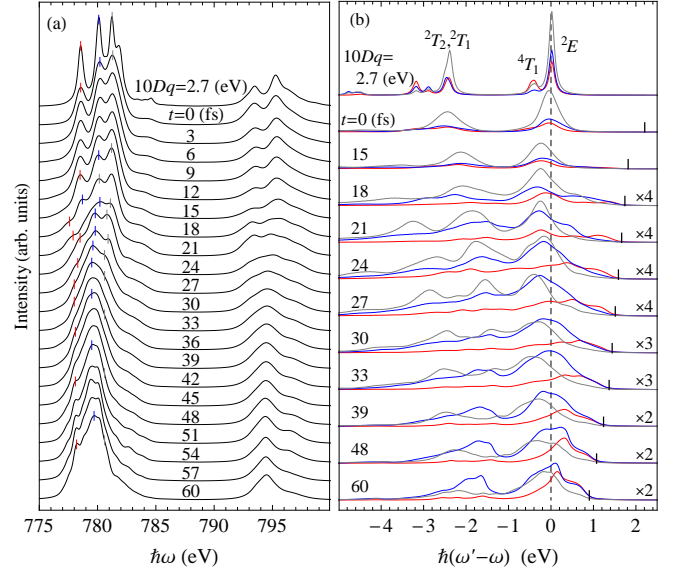

FIG. 2: The time-dependent nonequilibrium X-ray response functions for the cobalt ion. (a) X-ray absorption intensity as a function of incoming photon energy $\hbar\omega$ for selected times indicated in the Figure. The metal-ligand separation and total energy at these times can be found in Fig. 1. (b) RIXS intensity as a function of the change in photon energy $\hbar(\omega' - \omega)$ for selected times indicated in the Figure. RIXS was calculated for the incoming photon energies indicated by the small vertical lines of corresponding color in the absorption spectra in (a). Some spectra are scaled by the amount shown in the Figure. The small black vertical lines indicate the highest possible $\hbar(\omega' - \omega)$. The top spectra show an atomic multiplet calculations with a static cubic crystal field of $10Dq = 2.7$ eV.

tum dissipation, the spin crossover still occurs[15], but the total spin values are between 1.1 and 1.35 for the first 1 ps and never reach the expected value of $S = \frac{3}{2}$ for a quartet state. The behavior of the total energy (kinetic and potential) as a function of the expectation value of the metal-ligand distance is shown in Fig. 1. After a few oscillations around the new equilibrium position, the system settles in the lowest quartet state in approximately 150-200 fs. For $t > 200$ fs, the system further relaxes between the spin-orbit split manifolds arising from the $^4T_1$ state, which are separated by ~130 meV, see Fig. 1(b).

Let us now turn our attention to the X-ray response. The photoexcitation adds an e electron to the $|3d^6(^1A_1)\rangle$ ground state of cobalt creating $|3d^7(^2E)\rangle$ states (in Mulliken notation) with predominantly $t_2^6 e$ character, see Fig. 1(a). Figure 2 shows the XAS and RIXS at different times t after the photoexcitation. The spectrum at $t \cong 0$ can be compared with a multiplet calculation with a static cubic crystal field $10Dq = 2.7$ eV, which has a low-spin ground state. The peak positions and weights of the nonequilibrium spectra at $t = 0$ fs and the multiplet calculation compare well indicating that the two initial states are similar. However, there is a significantly larger broadening of the spectral features for the nonequilibrium system. The change in equilibrium metal-ligand

distances for divalent and trivalent cobalt leads to the formation of a coherent wave packet in the ^2E potential well. For a particular final state, the spectral weight of the n'th excited vibronic states is then given by the Poisson distribution $e^{-g}g^n/n!$, with $g = (E(0) - E_0(^2E))/(\hbar\omega_0) \cong 30$, where $E(t)$ is the energy of the nonequilibrium state and $E_0(^2E)$ is the minimum energy of the ^2E state. For large g, this can be approximated by $\exp[-(n-g)^2/(2g)]$ with a full-width-half-maximum of $2\sqrt{2g \ln 2}$ corresponding to an energy width of about 0.5 eV. This is close to the width of the RIXS zero-loss line, see Fig. 2(b).

In the following approximately 15 fs, the system moves in the ^2E potential well. The structure of the XAS and RIXS spectra remains similar to the $t = 0$ spectrum. Although RIXS does not conserve spin, as a rule of thumb, spin-flip transitions are suppressed relative to the spin-conserving transitions by a factor $(j + \frac{1}{2})^2 = 4, 1$, where $j = \frac{3}{2}, \frac{1}{2}$ is the $2p$ total angular momentum for the $L_{3/2}$ edges, respectively[27,35]. At the L_3 edge, the strongest peaks therefore arise from spin-conserving crystal-field transitions $(t_2 \rightarrow e)$. Starting from the predominantly $t_2^6 e$ initial state, this gives a $t_2^5 e^2$ configuration, which is present in several irreducible representations[26] that are split by the dd Coulomb interaction. The most dominant are the $^2T_1$ and $^2T_2$ states that are close in energy. The energy needed to make a $^2E \rightarrow^2 T_1, ^2T_2$ decreases strongly between 0 and 15 fs. The transition energy, which is somewhat less than the effective crystal field splitting, decreases due to the reduction in repulsion between the electrons on the cobalt and the ligands represented by the breathing mode.

The spin crossover occurs in the time range of 15-25 fs, when it reaches over 90% of the $S = \frac{3}{2}$ spin value[15]. One of the most noticeable features is the appearance of spectral weight on the energy-gain side in the RIXS spectra in Fig. 2(b). These anti-Stokes features have been observed experimentally in $Fe(CO)_5$[20]. Although energy-gain states are already present directly after photoexcitation, their intensity was strongly suppressed (the largest possible energy gain is indicated by the small black vertical lines in Fig. 2(b)). The reason for the small initial spectral weight is two-fold: first, the transition requires a spin flip, which has a smaller transition probability; second, the overlap between the two displaced states of the breathing mode is exponentially suppressed[36]. Another indicator of the intersystem crossing is the disappearance of sharp features in both XAS and RIXS. Note, for example, the extremely broad X-ray absorption spectrum at $t = 21$ fs in Fig. 2. The presence of a clear X-ray spectral line shape is the result of the combination of selection rules and a relatively well-defined initial state. The strong mixing between the doublet and quartet states during the spin crossover leads to a breakdown of the latter condition. Therefore, during the spin crossover, we also observe the appearance of quartet states. In particular, the RIXS features for energy losses greater than 3 eV, can be identified as $^4T_1$ states. This state has predominantly $t_2^4(^3T_1)e^3$ character and is a minority-
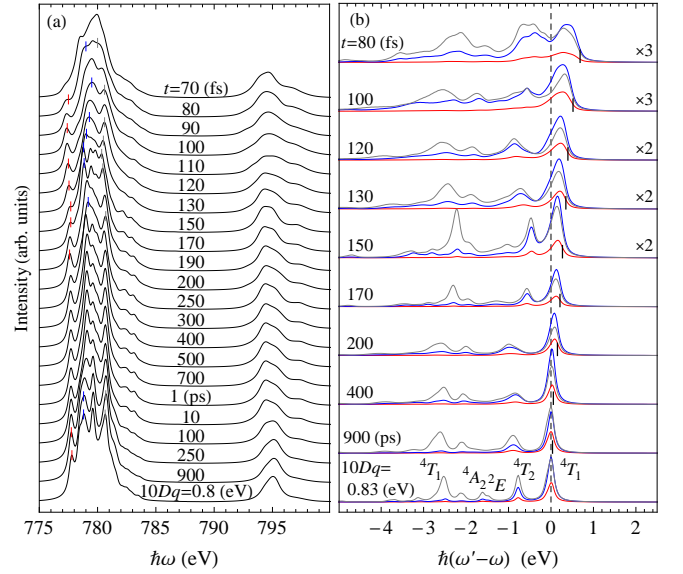

FIG. 3: Same as Fig. 2, but now for times from 70 fs to 900 ps. The bottom spectra are multiplet calculations with $10Dq = 0.83$ eV.

spin crystal-field excitation starting from the high-spin $^4T_1$ state.

In the time range after the spin crossover, from $t = 30$ to roughly 150 fs, the system relaxes into the lowest quartet state due to quantum dissipation. This is manifested in different ways in the X-ray response functions. First, there is a clear narrowing of the features in the XAS, see Fig. 2(a). Although spin is not a good quantum number due to the large $2p$ spin-orbit interaction, the XAS final states can still be grouped into states with a large quartet or doublet character. The narrowing occurs because there are simply less quartet states that are spread over a narrower energy range compared to the doublet states[37]. We return to the strong increase in the branching ratio (the intensity ratio of the L_3 and L_2 edges) below. The RIXS calculations also show a narrowing of the spectral features. The relaxation can also be seen in the energy-gain features which move closer to the zero-energy loss peak and increase in intensity. Additionally, there is an oscillation between 0.5 and 1 eV of the $^4T_2$ state, which follows the damped oscillatory motion of the breathing mode . This state corresponds to a $t_2 \rightarrow e$ crystal-field excitation starting from the $^4T_1$ state. The spectra for large times $t > 200$ ps still show additional phonon broadening, which is not related to motion of the breathing mode in the initial state, but to vibronic excitations created by the RIXS process[36].

We now discuss the further relaxation in the metastable $^4T_1$ state for $t > 150$ fs, see Fig. 3. First, let us note that the final XAS spectrum at $t = 900$ ps compares well with a ligand field calculation with cubic crystal field of $10Dq = 0.833$ eV, see Fig. 3(a). The value of $10Dq$ is equal to $\frac{1}{3}\varepsilon_p$, which is the expected energy difference due to the electron-phonon coupling between 1

and 2 e electrons. This agreement is not directly obvious considering the strong coupling between the electronic system and the breathing mode. However, as a result of the final-state mixing by the Coulomb and $2p$ spin-orbit interactions, the result is only a small broadening.

A crucial parameter of the isotropic L-edge XAS is the branching ratio (BR), *i.e.* the intensity ratio of the L_3 and L_2 edges, see the red line in Fig. 4. This quantity can provide information on the nonequilibrium state even when the spectra are significantly broadened. Without interactions, the expected statistical ratio is 2, which is the ratio of the degeneracies of the $2p_j$ core levels. Right after photoexcitation, the branching ratio is 1.44 and therefore less than statistical. During the spin crossover, the branching ratio increases quickly to 3 and then re-treats somewhat. After strong oscillations between 40 and 80 fs, the branching ratio increases steadily to close to 7.6. Clearly, the branching ratio is a sensitive quantity and reflects changes in the development of the excited state. Let us take a closer look at the effects underlying these changes. Sum rules relate the branching ratio to properties of the initial state[27,37],

$$\text{BR}(t) = \frac{I_{L_3}}{I_{L_2}} = \frac{2n_h - \langle\psi(t)|\mathbf{L}\cdot\mathbf{S}|\psi(t)\rangle + \beta(t)}{n_h + \langle\psi(t)|\mathbf{L}\cdot\mathbf{S}|\psi(t)\rangle - \beta(t)}, \quad (5)$$

where n_h is the number of holes with $n_h = 3$ for divalent cobalt. The factor $\beta(t)$ reflects the effect of Coulomb interactions on the branching ratio, to which we return below. Taking $\beta(t) = 0$ and no spin-orbit coupling gives the statistical ratio. The next term is the expectation value in the nonequilibrium state of the angular part of the spin-orbit coupling $\langle\psi(t)|\mathbf{L}\cdot\mathbf{S}|\psi(t)\rangle$. The gray line in Fig. 4 shows the expected branching ration for $\beta(t) = 0$. Although the absolute value is off, the isotropic branching ratio from the spectra reflects well the variations of the spin-orbit coupling in the nonequilibrium state.

The derivation of the sum rule for the isotropic spectrum in Eq. (5) (with $\beta(t) = 0$) assumes that the j value of the core level is a good quantum number. Unfortunately, this is not the case for divalent cobalt where Coulomb interactions couple the spin-orbit split edges. Therefore, although variations in the spin-orbit coupling in the $3d$ levels are reflected in the branching ratio, additional corrections are needed to explain the absolute value. The additional effects due to the Coulomb interaction are modeled phenomenologically with the term $\beta(t)$. In the excited state, the Coulomb interaction in the $3d$ shell steadily decreases when going from the low-spin state to the Hund's rule stabilized ground state. This also affects the X-ray absorption final state[37]. Since the dipole transition is spin conserving, low/high-spin states end up in final states with predominantly low/high spin character, which, on average, have a higher/lower aborption energy[37], respectively. When the final states are split by the large $2p$ spin-orbit interaction, this leads to lower/higher branching ratio for the low/high spin initial states, respectively. Since the Coulomb interaction is lowered in going from low-to-high spin followed by a
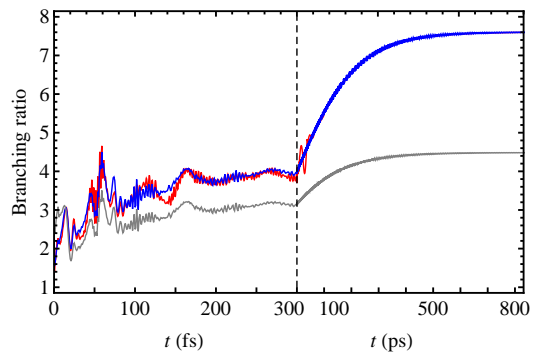

FIG. 4: The red line shows the isotropic branching ratio obtained from the calculated isotropic X-ray absorption. The gray and blue line show the expected branching ratio obtained from the nonequilibrium state $|\psi(t)\rangle$ using Eq. (5) without and with the effects of the Coulomb interaction, respectively.

decay among quartet states, we expect the branching ratio to increase as a function of time. This trend is the same as for the spin-orbit coupling, where, for more than half-filled shells, the spin and orbit are expected to be coupled parallel. Modeling the Coulomb term as $\beta(t) = 0.12 + 0.78e^{-t/\tau}$ with $\tau \cong 100$ ps significantly improves the agreement, see the blue line in Fig. 4. This smooth varying correction works well when the initial state is predominantly in the high-spin quartet states. However, a different dependence is necessary in the spin crossover region where the Coulomb interaction changes rapidly and Equation (5) with $\beta(t) = 0$ initially underestimates the branching ratio due to the low-spin character of the initial state and, after the spin cross into the high-spin state, overestimates the branching ratio. In Fig. 4, a correction of $\beta(t) = -0.9 + 0.51t$ is used during the spin crossover ($t < 20$ fs).

The effects on the branching ratio can therefore be summarized as follows. Directly after the photoexcitation, the branching ratio is less than the statistical value of 2, indicative of the low spin state. During the spin crossover, it starts to exceed the statistical value when entering the quartet states. Between 40 and 80 fs, the branching ratio fluctuates strongly with a maximum value occuring around $\frac{1}{2}T_0 \cong 52$ fs, where $T_0 = 2\pi/\omega_0 = 103$ fs is the oscillation period of the breathing mode. This region corresponds to the maximum metal-ligand distance, see Fig. 1(b), and mixing with other quartet states ($^4T_2$, $^4A_2$) occurs[15]. These multiplets have a higher number of t_2 holes which are more likely to form a finite angular momentum and therefore enhance the expectation value of the spin-orbit coupling thereby increasing the branching ratio. The mixing with other quartet states decreases due to the damping of the oscillation of the breathing mode, but smaller enhancements of the branching ratio are still observed at $\frac{3}{2}T_0 \cong 155$ and $\frac{5}{2}T_0 \cong 258$ fs.

After the spin crossover and the initial relaxation into the $^4T_1$ state, the next phase is the long-term relaxation between the spin-orbit split manifolds of the $^4T_1$ state,

see Fig. 1(b). The splitting can be understood intuitively by taking the threefold degeneracy of the T_1 irreducible representation as an effective angular momentum $\mathbf{L}_{\text{eff}} = 1$. This is then coupled to the $S = \frac{3}{2}$ spin giving $J_{\text{eff}} = \frac{5}{2}, \frac{3}{2}, \frac{1}{2}$. In a cubic symmetry, the $J_{\text{eff}} = \frac{5}{2}$ state further splits into two- and fourfold degenerate irreducible representations. The twelvefold-degenerate $^4T_1$ state therefore splits into the irreducible representations E', U', U', and E''[26], see Fig. 1(b). The corresponding spin-orbit coupling is $\langle \mathbf{L} \cdot \mathbf{S} \rangle = -1.39, -0.82, 0.08,$ and $0.60\ \hbar^2$, respectively. The long-term behavior of the branching ratio can be understood by a slow decay among the spin-orbit split states of the $^4T_1$ irreducible representation. Since the Coulomb interaction hardly changes, *i.e.* $\beta(t)$ remains constant, the increase in branching ratio is mainly due to the change in $\langle \mathbf{L} \cdot \mathbf{S} \rangle$.

V. DISCUSSION

Whereas recent years have seen tremendous progress in the development of well-defined short-pulsed soft-X-ray sources, little is known about the time-dependent soft-X-ray response of a nonequilibrium system. This paper provides a framework for key aspects to consider for time-dependent X-ray spectroscopy. The first thing to note is the wealth of information contained in the spectra which cannot be described as a simple superposition of the initial and metastable state spectra as measured in transient X-ray spectroscopy on the relatively long-lived metastable state[38–40]). The X-ray absorption at transition-metal L edges provides a strong sensitivity to changes in the local symmetry and spin. The strong mixing during the intersystem crossing (the spin crossover in the Prussian blue analogue) leads to an apparent breakdown of selection rules. Even relatively detailed changes due to small interactions such as the spin-orbit interaction (an essential interaction for the spin crossover) cause significant changes in the isotropic branching ratio, which can be interpreted using a combination of sum rules and spectral analysis. The RIXS spectra give a more direct insight into changes in the local electronic structure. The creation of a coherent wave packet is reflected in the broadening of the spectral line shape. This motion is further reflected in the crystal-field collapse and following oscillations caused by the change in metal-ligand distance. The spin crossover also manifests itself by the strong time-dependent spectral weight of the energy-gain features.

* Electronic address: veenendaal@niu.edu
[1] B. W. J. McNeil and N. R. Thompson, Nature Photon. **4**, 814 (2010).
[2] E. Allaria, D. Castronovo, P. Cinquegrana, P. Craievich, M. Dal Forno, M. B. Danailov, G. D'Auria, A. Demidovich, G. De Ninno, S. Di Mitri, et al., Nature Photon. **7**, 913 (2013).
[3] D. Ratner, R. Abela, J. Amann, C. Behrens, D. Bohler, G. Bouchard, C. Bostedt, M. Boyes, K. Chow, D. Cocco, et al., Phys. Rev. Lett. **114**, 054801 (2015).
[4] P. Gütlich and H. A. Goodwin, eds., *Spin crossover in Transition-Metal Compounds* (Springer, 2004).
[5] A. Bousseksou, G. Molnar, L. Salmon, and W. Nicolazzi, Chem. Soc. Rev. **40**, 3313 (2011).
[6] A. Hauser, *Spin crossover materials: Properties and application* (Wiley, 2013).
[7] P. Gütlich, Y. Garcia, and T. Woike, Coordination Chemistry Reviews **219-221**, 839 (2001).
[8] G. Auböck and M. Chergui, Nat. Chem. **7**, 629 (2015).
[9] C. Bressler, C. Milne, V.-T. Pham, A. ElNahhas, R. M. van der Veen, W. Gawelda, S. Johnson, P. Beaud, D. Grolimund, M. Kaiser, et al., Science **323**, 489 (2009).
[10] N. Huse, H. Cho, K. Hong, L. Jamula, F. M. F. de Groot, T. K. Kim, J. K. McCusker, and R. W. Schoenlein, The Journal of Physical Chemistry Letters **2**, 880 (2011).
[11] W. Zhang, R. Alonso-Mori, U. Bergmann, C. Bressler, M. Chollet, A. Galler, W. Gawelda, R. G. Hadt, R. W. Hartsock, T. Kroll, et al., Nature **509**, 345 (2014).
[12] M. Cammarata, R. Bertoni, M. Lorenc, H. Cailleau, S. Di Matteo, C. Mauriac, S. F. Matar, H. Lemke, M. Chollet, S. Ravy, et al., Phys. Rev. Lett. **113**, 227402 (2014).
[13] O. Sato, T. Iyoda, A. Fujishima, and K. Hashimoto, Science **272**, 704 (1996).
[14] T. Kawamoto, Y. Asai, and S. Abe, Phys. Rev. Lett. **86**, 348 (2001).
[15] M. van Veenendaal, Sci. Rep. **7**, 6672 (2017).
[16] M. Kabir and K. J. Van Vliet, Phys. Rev. B **85**, 054431 (2012).
[17] T. Kroll, J. Kern, M. Kubin, D. Ratner, S. Gul, F. D. Fuller, H. Löchel, J. Krzywinski, A. Lutman, Y. Ding, et al., Opt. Express **24**, 22469 (2016).
[18] M. Kubin, J. Kern, S. Gul, T. Kroll, R. Chatterjee, H. Lchel, F. D. Fuller, R. G. Sierra, W. Quevedo, C. Weniger, et al., Structural Dynamics **4**, 054307 (2017).
[19] P. Wernet, K. Kunnus, I. Josefsson, I. Rajkovic, W. Quevedo, M. Beye, S. Schreck, S. Grubel, M. Scholz, D. Nordlund, et al., Nature **520**, 78 (2015).
[20] K. Kunnus, I. Josefsson, I. Rajkovic, S. Schreck, W. Quevedo, M. Beye, S. Grbel, M. Scholz, D. Nordlund, W. Zhang, et al., New Journal of Physics **18**, 103011 (2016).
[21] C. Milne, T. Penfold, and M. Chergui, Coordination

Chemistry Reviews **277-278**, 44 (2014), ISSN 0010-8545.

[22] T. J. Penfold, M. Papai, T. Rozgonyi, K. B. Moller, and G. Vanko, Faraday Discuss. **194**, 731 (2016).

[23] G. Capano, C. J. Milne, M. Chergui, U. Rothlisberger, I. Tavernelli, and T. J. Penfold, Journal of Physics B: Atomic, Molecular and Optical Physics **48**, 214001 (2015).

[24] S. P. Neville, V. Averbukh, S. Patchkovskii, M. Ruberti, R. Yun, M. Chergui, A. Stolow, and M. S. Schuurman, Faraday Discuss. **194**, 117 (2016).

[25] M. van Veenendaal, J. Chang, and A. J. Fedro, Phys. Rev. Lett. **104**, 067401 (2010).

[26] J. S. Griffith, *The Theory of Transition-Metal Ions* (Cambridge University Press, Cambridge, 1961).

[27] M. van Veenendaal, *The Theory of Inelastic Scattering and Absorption of X-rays* (Cambridge University Press, Cambridge, 2015).

[28] S. Bonhommeau, N. Pontius, S. Cobo, L. Salmon, F. M. F. de Groot, G. Molnar, A. Bousseksou, H. A. Durr, and W. Eberhardt, Phys. Chem. Chem. Phys. **10**, 5882 (2008).

[29] M. L. Baker, Y. Kitagawa, T. Nakamura, K. Tazoe, Y. Narumi, Y. Kotani, F. Iijima, G. N. Newton, M. Okumura, H. Oshio, et al., Inorganic Chemistry **52**, 13956 (2013).

[30] I. Jarrige, Y. Q. Cai, H. Ishii, N. Hiraoka, and A. Bleuzen, Applied Physics Letters **93** (2008).

[31] M. Magnuson, S. M. Butorin, J.-H. Guo, and J. Nordgren, Phys. Rev. B **65**, 205106 (2002).

[32] S. G. Chiuzbăian, T. Schmitt, M. Matsubara, A. Kotani, G. Ghiringhelli, C. Dallera, A. Tagliaferri, L. Braicovich, V. Scagnoli, N. B. Brookes, et al., Phys. Rev. B **78**, 245102 (2008).

[33] L. J. P. Ament, M. van Veenendaal, T. P. Devereaux, J. P. Hill, and J. van den Brink, Rev. Mod. Phys. **83**, 705 (2011).

[34] M. Hochbruck and C. Lubich, SIAM Journal on Numerical Analysis **34**, 1911 (1997).

[35] M. van Veenendaal, Phys. Rev. Lett. **96**, 117404 (2006).

[36] L. J. P. Ament, M. van Veenendaal, and J. van den Brink, Europhys. Lett. **95**, 27008 (2011).

[37] B. T. Thole and G. van der Laan, Phys. Rev. B **38**, 3158 (1988).

[38] M. Saes, C. Bressler, R. Abela, D. Grolimund, S. L. Johnson, P. A. Heimann, and M. Chergui, Phys. Rev. Lett. **90**, 047403 (2003).

[39] N. Huse, T. K. Kim, L. Jamula, J. K. McCusker, F. M. F. de Groot, and R. W. Schoenlein, Journal of the American Chemical Society **132**, 6809 (2010).

[40] L. X. Chen and X. Zhang, The Journal of Physical Chemistry Letters **4**, 4000 (2013).